Ultrasoft magnetic films investigated with Lorentz transmission electron microscopy and electron holography

de Hosson, J.T.M.; Chechenin, N.G.; Alsem, D.H.; Vystavel, T.; Kooi, B.J.; Chezan, A.R; Boerma, D.O

Published in:
Microscopy and Microanalysis

DOI:
10.1017/s1431927602020214

Microsc. Microanal. 8, 274–287, 2002
DOI: 10.1017.S1431927602020214

Microscopy AND Microanalysis

Ultrasoft Magnetic Films Investigated with Lorentz Tranmission Electron Microscopy and Electron Holography

Jeff Th.M. De Hosson,* Nicolai G. Chechenin, Daan-Hein Alsem, Tomas Vystavel, Bart J. Kooi, Antoni R. Chezan, and Dik O. Boerma

Department of Applied Physics, Materials Science Center and Netherlands Institute for Metals Research, University of Groningen, Nijenborgh 4, 9747 AG Groningen, The Netherlands

Abstract: As a tribute to the scientific work of Professor Gareth Thomas in the field of structure-property relationships this paper delineates a new possibility of Lorentz transmission electron microscopy (LTEM) to study the magnetic properties of soft magnetic films. We show that in contrast to the traditional point of view, not only does the direction of the magnetization vector in nano-crystalline films make a correlated small-angle wiggling, but also the magnitude of the magnetization modulus fluctuates. This fluctuation produces a rapid modulation in the LTEM image. A novel analysis of the ripple structure in nano-crystalline Fe-Zr-N film corresponds to an amplitude of the transversal component of the magnetization ΔM_y of 23 mT and a longitudinal fluctuation of the magnetization of the order of $\Delta M_x = 30$ mT. The nano-crystalline $(Fe_{99}Zr_1)_{1-x}N_x$ films have been prepared by DC magnetron reactive sputtering with a thickness between 50 and 1000 nm. The grain size decreased monotonically with N content from typically 100 nm in the case of N-free films to less than 10 nm for films containing 8 at%. The specimens were examined with a JEOL 2010F 200 kV transmission electron microscope equipped with a post column energy filter (GIF 2000 Gatan Imaging Filter). For holography, the microscope is mounted with a biprism (JEOL biprism with a 0.6 μm diameter platinum wire).

Key words: Lorentz microscopy, electron holography, magnetic properties, nano-crystalline Fe-Zr-N film

Introduction

A prominent contribution to the field of materials science was made by the advent of transmission electron microscopy. In the early 1960s, Professor Gareth Thomas stood on the threshold of this development (Thomas and Goringe, 1979) and indisputably he became an inspiring and enthusiastic world leader in the application of this technique to solve materials problems. Only a few of us have pioneered so much in the structure-property relationship and in so many different areas of materials science. His research covered an extraordinarily broad range of topics, but it was and still is characterized by a deep penetration into each subject to provide a thorough understanding. His seminal work stimulated hundreds of investigations over the last 40 years, clarifying structural aspects and thereby permitting analysis of the structural properties. Through these studies, our understanding of the relationship between microstructure and property became more satisfactory and new concepts have been developed further. Besides structural properties, Thomas showed great interest in the application of transmis-

Received March 14, 2002; accepted April 4, 2002.

*Corresponding author

sion electron microscopy to the field of functional materials. For instance, he focused on a connection between the microstructure of various nano-structured alloys and the giant magneto-resistive (GMR) properties (Berkowitz et al., 1992; Hütten et al., 1995) that also stimulated later our own scientific work (Kooi et al., 2001; Vrenken et al., 2001).

Along these lines of his own interests, this contribution concentrates on the application of transmission electron microscopy to functional materials, such as ultrasoft magnetic films for high-frequency inductors, to reveal the structure-property relationship. There exists an increasing demand for further miniaturization in portable appliances (e.g., mobile phones, palmtops), that is to say in communication tools. To this end, the use of high frequencies (e.g., 10–1000 MHz) in combination with thin magnetic materials is desirable. The use of magnetic films allows the integration of transformers and inductors into silicon IC circuitry. Soft magnetic films are also widely used in modern electromagnetic devices as a high-frequency (>100 MHz) field-amplifying component, for example, in read–write heads for magnetic disk memories for computers and as a magnetic shielding material, for example in tuners. The main requirements for the film material are a high saturation magnetization combined with a low coercivity and a small but finite anisotropy field. In addition, the material should have a reasonably high specific electrical resistivity to reduce eddy currents, and also appropriate mechanical properties. To obtain the desired properties (low coercivity, little strain, and very small magnetostriction), the use of materials with a grain size of the order of 10 nm, like nano-crystalline iron-based materials, becomes attractive.

Knowledge of local magnetic properties is essential for the development of new magnetic nano-sized materials. One of techniques that is suitable for the measurement of local magnetic structures is the Lorentz–Fresnel (or defocused) imaging mode of the transmission electron microscope. This rather classical TEM technique (Fuller and Hale, 1960; Grundy and Tebble, 1968) has several outstanding advantages: uncomplicated application to various parts of thin foil, the possibility of dynamical studies, and good spatial resolution. Nevertheless, obtaining quantitative information from Lorentz micrographs is relatively difficult due to an indirect link between image contrast and the spatial variation of the magnetic induction, which is problematic in regions of abrupt magnetization changes (De Graef, 2000).

In this paper, the possibility of a quantitative analysis of the magnetic properties of nano-crystalline iron using transmission electron microscopy is presented. The goal is to delineate a more quantitative way to obtain information about the magnetic induction and local magnetization. In particular, the latter physical quantities affect the functional properties of ultrasoft magnetic materials for high-frequency inductors. One of the magnetic features that can provide quantitative magnetic information is the so-called magnetization or magnetic ripples, caused by local variation of magnetic induction that deviate from the mean magnetization direction (Hoffmann, 1964). Lorentz–Fresnel (LTEM) and (off-axis) electron holographic modes are used to analyze the magnetic structures.

Experimental Results

Nano-crystalline Fe-Zr-N films have been prepared by DC magnetron reactive sputtering with a thickness between 50 and 1000 nm. The presence of zirconium is to catch the nitrogen in the iron matrix. Iron was chosen because it is easy to prepare and cheaper than other soft magnetic materials, for example, cobalt. The nitrogen is added to get a small (nano-sized) grain size. Pure (99.96 at%) Fe sheets partially covered with Zr wires were used as targets. The N and Zr contents were controlled by varying the sputter power and/or the Ar/N_2 gas mixture. An 800-Oe magnetic field was applied in the plane of the samples during deposition. More details on the film deposition can be found in Chezan et al. (2002).

The films have been deposited on glass or silicon substrates at several temperatures between room temperature and 200°C. The DC-sputtered samples were deposited on either a silicon substrate covered by a polymer, which was removed in acetone after sputtering, or on a silicon substrate covered by a Si_3N_4 layer. The former samples were extracted on copper TEM-grids for support, while the latter samples kept their substrate because the layers were very thin. Because all the films are sputtered or electrochemically deposited, they are of uniform thickness. The deposition conditions were chosen to obtain a composition $(Fe_{99}Zr_1)_{1-x}N_x$, where the concentration of nitrogen was in the range $x \leq 25$ at%. The best films as far as nano-size dimensions are concerned have been obtained for 8 at% $< x <$ 20 at%. The nitrogen concentration has been measured with an elastic recoil detection technique, neutron depth profiling methods, and compared with shifts in the XRD pattern. Standard $\theta - 2\theta$ XRD scans showed that up to $x = 10$ at% as sputtered films

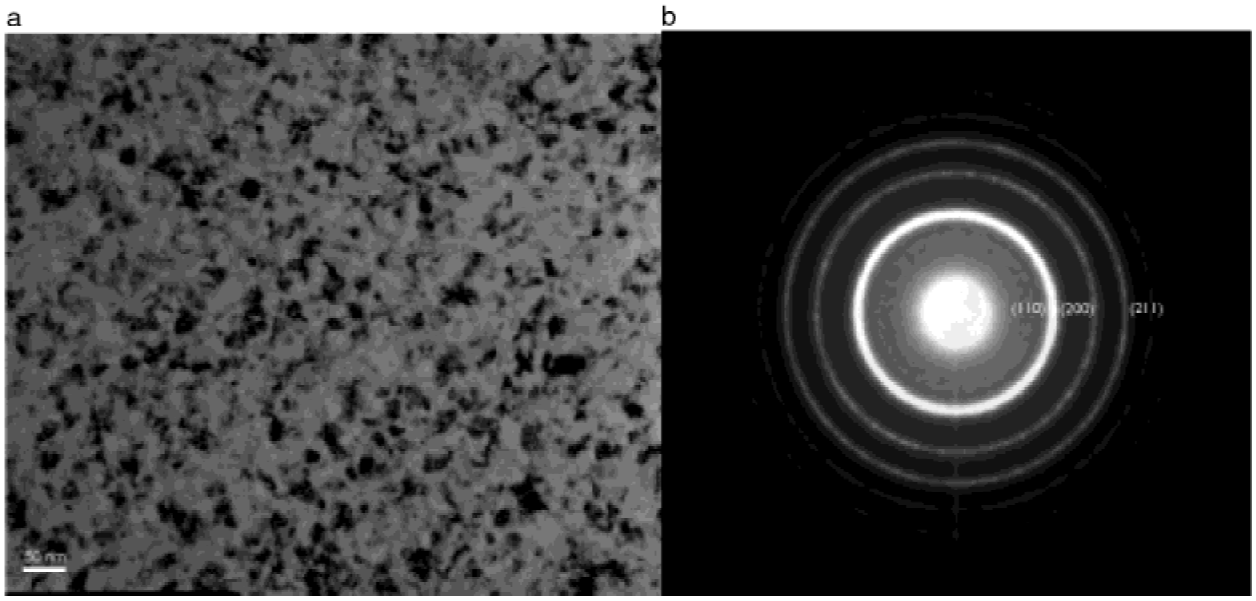

Figure 1. Nano-crystalline iron (**a**) and SA diffraction pattern of nano-crystalline $Fe_{94}N_5Zr_1$ (**b**).

were BCC single-phase materials with a strong (110) fiber texture. The grain size, estimated from the width of the (110) peak, decreased monotonically with N content from typically 100 nm in the case of N-free films to less than 10 nm for films containing 8 at%.

The specimens were examined with a JEOL 2010F 200-kV transmission electron microscope equipped with a post column energy filter (GIF 2000 Gatan Imaging Filter, with a resolution of 1024×1024 pixels), which provides an additional magnification around 20 at the plane of CCD camera with respect to the maximal attainable magnification by using the objective minilens (magnification: 6×10^3). For holography, the microscope is mounted with a biprism (JEOL biprism with a 0.6 μm diameter platinum wire). Grain size determination was done with several tilting experiments using an ACT (automated crystallography) for the TEM, from TSL/EDAX, and a Gatan dual-view CCD camera (resolution 1300×1030 pixels). A single-tilt specimen holder and a double-tilt heating specimen holder were used. The images are acquired and edited using DigitalMicrograph (DM) 3.3 and 3.4 on both Apple Macintosh and Microsoft Windows PCs. Furthermore, an additional script package for DM was used: the NCEM Package Image that was developed at the national center for electron microscopy founded by Thomas at the Lawrence-Berkeley National Laboratory in the United States.

XRD, as well as conventional TEM and selected area diffraction (SAD), reveal a 2–30 nm size of crystallites after various tilting experiments for most of the investigated sputter deposited films (see Fig. 1) and in the diffraction pattern of Figure 1b, the allowed reflections for the bcc structure were found (110, 200, 211). No signs of Fe_4N or $Fe_{16}N_2$ were detected in XRD. A very weak ring within the first bright ring can be observed that originates from an oxide layer on the surface. The average measured grain size is approximately 34 nm as shown in Figure 2. The grain size distribution is rather broad, even for sputtered films. Indeed, one should be careful with this analysis when the film thickness is much larger than the grain size. The information of more grains on top of each other may cause the ACT to measure an incorrect grain size and a different orientation distribution. It should be stressed that the grain size distribution depends on the exact condition of the deposition process, that is, on the nitrogen concentration. There are many defects in individual grains. With *in situ* annealing up to 250°C, the grain size distribution becomes sharper and this phenomenon is related to the crystallization of the intergranular amorphous-like phase.

Figure 3 shows three domain walls and the magnetic ripples within the different grains as observed in LTEM (objective lens turned down) and Figure 4 shows a cross-tie wall. Because the magnetization is perpendicular to the magnetic ripple structure within the magnetic domains, magnetic induction vectors can be drawn in the image(s) (Figs. 3 and 4). Figure 3 shows that there are two 90° Néel domain walls, which is to be expected in thin films like

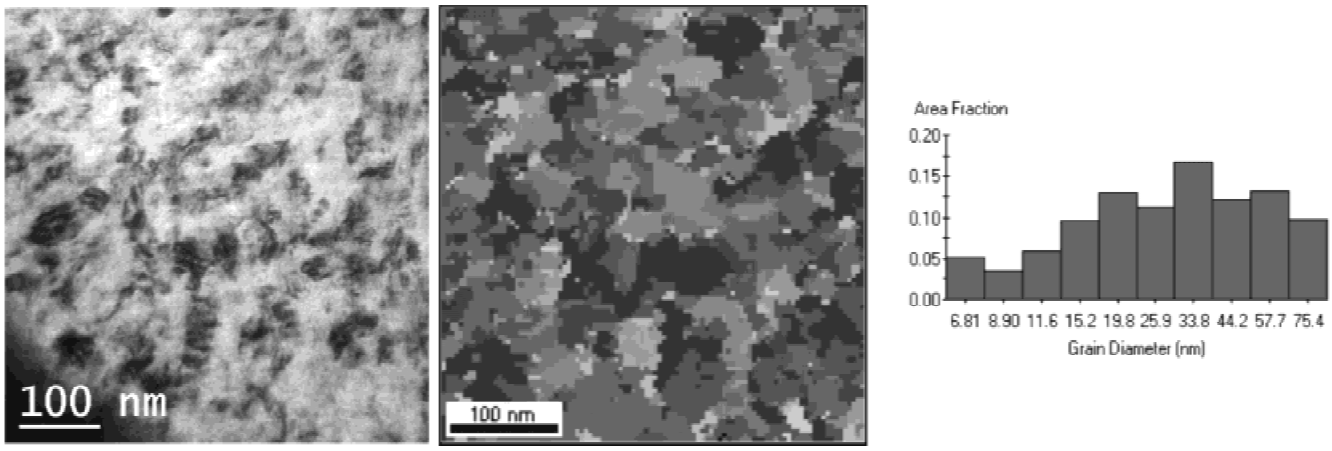

Figure 2. Grain size and grain size distribution from ACT300 analysis (automated crystallography for the TEM, from TSL/EDAX).

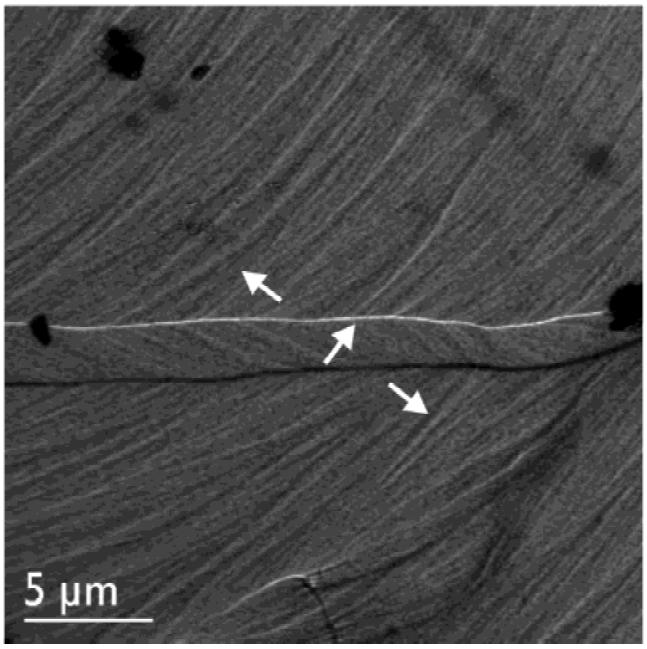

Figure 3. Magnetization direction within magnetic domains.

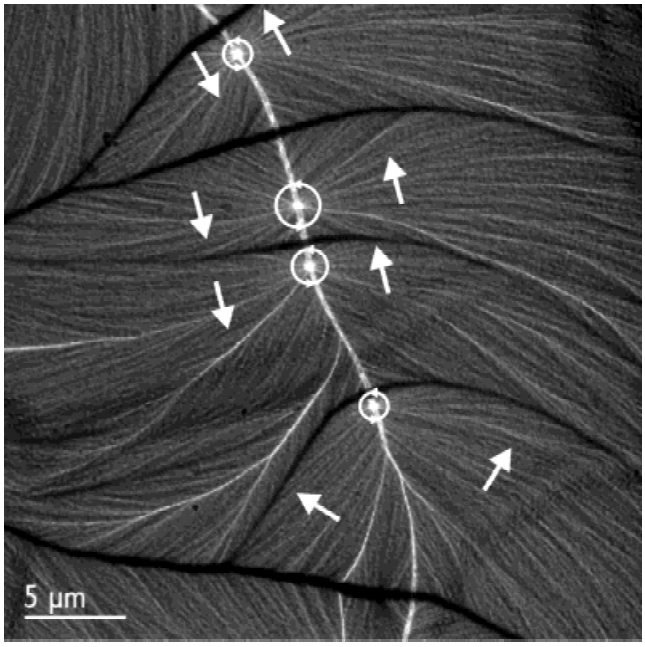

Figure 4. Magnetization direction in a cross-tie wall.

these. The magnetic ripples are characterized by the mean wavelength and the mean angle of deviation of the local magnetization variation. These could be scrutinized by a careful analysis of the Lorentz images in Fourier space. A typical magnetic contribution in frequency domain of a ripple structure is represented by a "bow tie"-like feature (see Fig. 5). To find the ripple wavelength, the dominant frequency in the frequency domain has to be found, whereas the deviation angle can be found by determining the (half) angle of the bow tie (angle θ in Fig. 5). The procedure of image analysis is as follows and displayed in Figure 6. First, an image containing homogeneous ripples is acquired. To determine the ripple wavelength, the rotational average of the modulus of the fast Fourier transform (FFT) is calculated (Fig. 6B, C). If a line profile from the center of the image is taken, the wavelength can be determined. This is done by looking at the first order maximum (indicated by a vertical line in Fig. 6D). Using the distance between this peak and the central peak, the average ripple wavelength can be calculated (Herrmann et al., 1994).

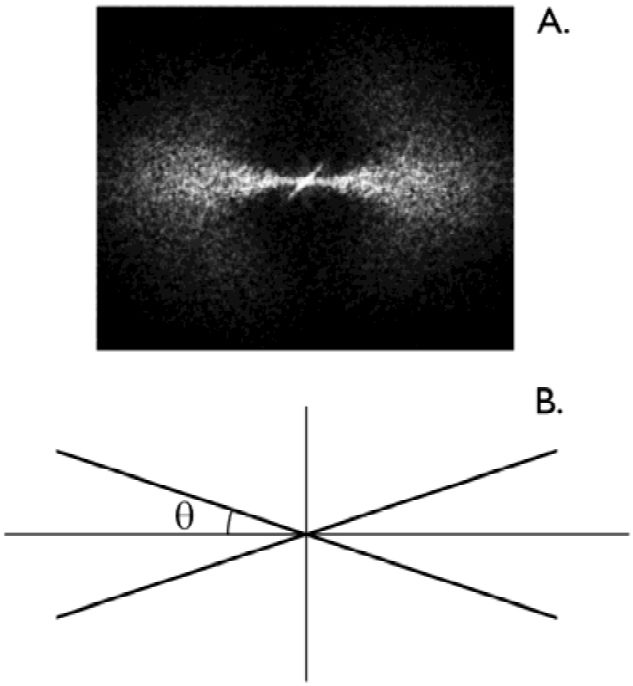

Figure 5. Typical diffractogram of the magnetic ripple structure.

The deviation angle of the ripple spectrum can also be found by calculating the modulus of the FFT (Gillies et al., 1995). The FFT contains two triangular shapes, from which the mean deviation angle can be obtained (Fig. 6). A band-pass mask is applied on the FFT at the distance from the origin where the first order maximum lies. Then a rotational profile is taken within this filtered FFT. Then, the ratio between the peak width (indicated by the rectangular shape in Fig. 6F) and the entire profile determines the angle. The peak width is determined by looking at the maximum intensity and by finding the points where the intensity falls to $\frac{1}{2}\sqrt{2}$ ($\approx$70%) of the maximum intensity.

An alternative transmission electron microscopy technique for obtaining information of the magnetization is electron holography, which is based on recording an interference pattern from which both the amplitude and phase of an object can be reconstructed (Gabor, 1949; Tonomura, 1999). Magnetic thin films are strong phase objects and the phase shift of the electrons passing through the specimen is proportional to the magnetic flux enclosed by the electron paths. There are various electron holographic techniques (Cowley, 1992), but one of the most popular is off-axis electron holography. The early holograms were limited to the brightness and with that to the coherence of the filament sources. The development of the field emission gun (FEG), which gives a coherent beam with a high intensity, contributed greatly to the implementation of electron holography in practice. For off-axis holography, a specimen is chosen that does not completely fill the image plane (e.g., a small magnetic element or the edge of an extended film) so that only part of the electron beam passes through the specimen. An electrostatic biprism, a thin (<1 μm) metallic wire or quartz fiber coated with platinum (or gold), is then used to recombine the specimen beam and the reference beam so that they interfere and form a hologram. This can be digitized and digital image-processing techniques can be applied to reconstruct an image of the magnetic domain structure. The intensity of the recorded hologram can be written as

$$\begin{aligned} I(x,y) &= |\Psi_1(x,y)|^2 + |\Psi_2(x,y)|^2 \\ &\quad + |\Psi_1(x,y)||\Psi_2(x,y)|[e^{i(\phi_1-\phi_2)} + e^{-i(\phi_1-\phi_2)}] \\ &= A_1^2 + A_2^2 + 2A_1A_2\cos\Delta\phi \end{aligned} \tag{1}$$

where Ψ is an electron wave function, ϕ represents the phase, and the subscripts refer to the reference and object waves, which travel through the opening and the specimen, respectively. Equation (1) shows that the phase and the amplitude information are enclosed in the holographic image (McCartney et al., 2000). The phase can be numerically reconstructed according to the following procedure. First, the fast Fourier transformation (FFT) of the holographic image (Fig. 7A) is taken (Fig. 7B). In the frequency domain, two sidebands can be detected. If one of the two side bands of the FFT is cut out and centered (Fig. 7C) and the inverse FFT of this centered sideband is taken, the phase will appear (Fig. 7D). Because one of the off-axis sidebands is centered to obtain the phase information, the method is called off-axis holography.

After a holographic image has been produced and the phase has been extracted, it has to be processed before the in-plane magnetic information perpendicular to the electron beam can be extracted in an induction map. First, the phase of the image has to be known to get magnetic information (Fuller and Hale, 1960; Midgley, 2001). If neither **B** or V vary with the penetration depth z, and neglecting magnetic and electric fields outside the sample, then the phase becomes

$$\begin{aligned} \varphi(x,y) &= C_E V(x,y)t(x,y) \\ &\quad - \frac{e}{\hbar}\iint \mathbf{B}_\perp(x,y)t(x,y)\,dx\,dy. \end{aligned} \tag{2}$$

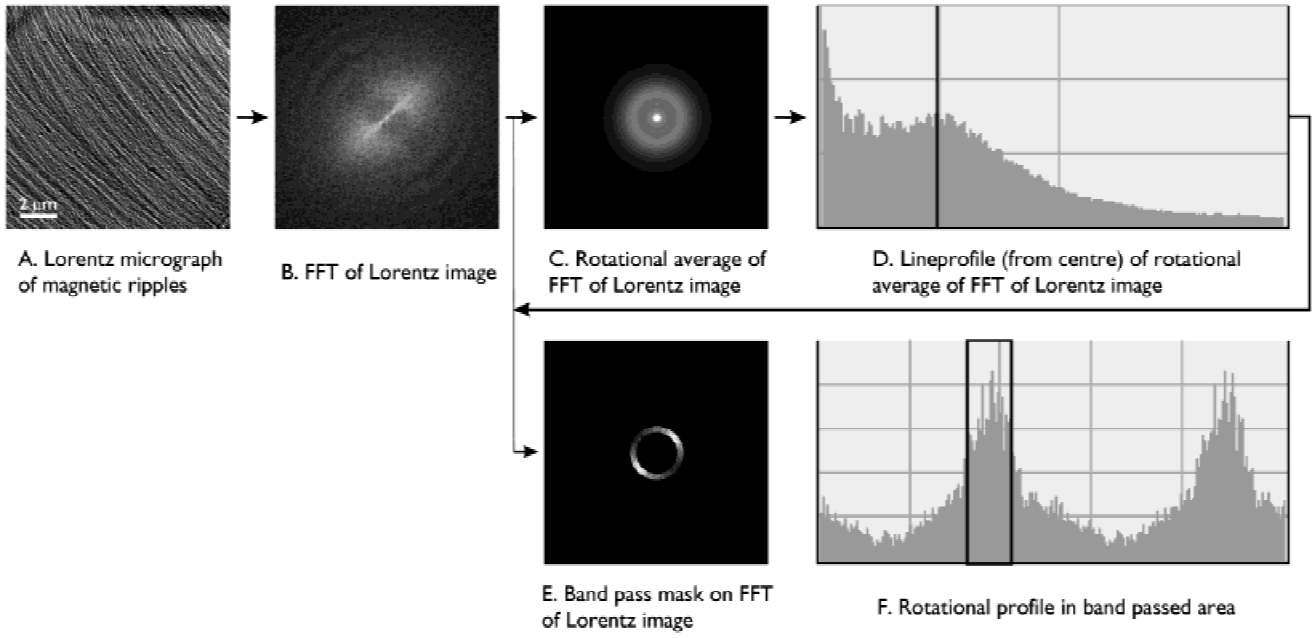

Figure 6. Schematic description of the quantification method.

In one dimension, equation (2) reads

$$\frac{d\varphi(x)}{dx} = C_E \frac{d}{dx}\{V(x)t(x)\} - \frac{e}{\hbar}\mathbf{B}_\perp(x)t(x), \qquad (3)$$

where $V(x)$ is the mean crystal potential, $t(x)$ represents the thickness as a function of the place, and $B_\perp$ is the component of the magnetic induction perpendicular to both x and z. Assuming that the thickness is constant over the whole image (because sputtered films are used, this assumption can be made) and the composition is homogeneous, the first right-hand-side term drops and only the second term remains. With Maxwell's equation $\nabla\cdot\mathbf{B} = 0$, $B_\perp$ can be split and written as

$$B_\perp(x,y) = B_x(x,y) + B_y(x,y)\begin{cases} B_x(x,y) = \dfrac{h}{2\pi et}\dfrac{d\varphi(x,y)}{dy} \\ B_y(x,y) = -\dfrac{h}{2\pi et}\dfrac{d\varphi(x,y)}{dx} \end{cases}. \qquad (4)$$

In summary, provided the phase is fully recovered, the derivative of the phase multiplied by a constant will give the magnetic induction in the x and y direction as a function of the position in the holographic image. To obtain the correct values for the magnetic induction, the unwrapped phase of the hologram is needed. To convert the phase to the unwrapped phase, the 2π steps have to be removed. This can be done by looking at the phase steps along a row or column of pixels in the image and by adding or subtracting 2π where appropriate.

In Figure 8, an electron hologram and its (unwrapped) reconstructed phase of the nano-crystalline Fe film is shown. When the phase and the Lorentz–Fresnel image of this cross-tie wall are compared in Figure 8, it can be seen that the cross-ties inside the cross-tie wall in both Lorentz–Fresnel and holography modes are clearly visible. To calculate the in-plane magnetic induction, the derivative of the phase has to be calculated and multiplied by the proper constants. The procedure is delineated in Figure 9. To calculate the magnetization from the phase, the unwrapped phase has to be calculated first (Midgley, 2001). Consequently, the image has to be free of singularities. Because a part of the images is free of singularities, only a smaller area can be observed and analyzed. Depending on the frame of reference chosen, the light or the dark areas show a higher value for the local magnetic induction. In Figure 9A, a higher intensity value represents a higher value for the magnetic induction. In Figure 10, another example of the reconstructed phase of nano-crystalline iron is shown. In this case, there is also magnetic contrast outside the sample (light area), which means that there is also a magnetic flux present outside the sample.

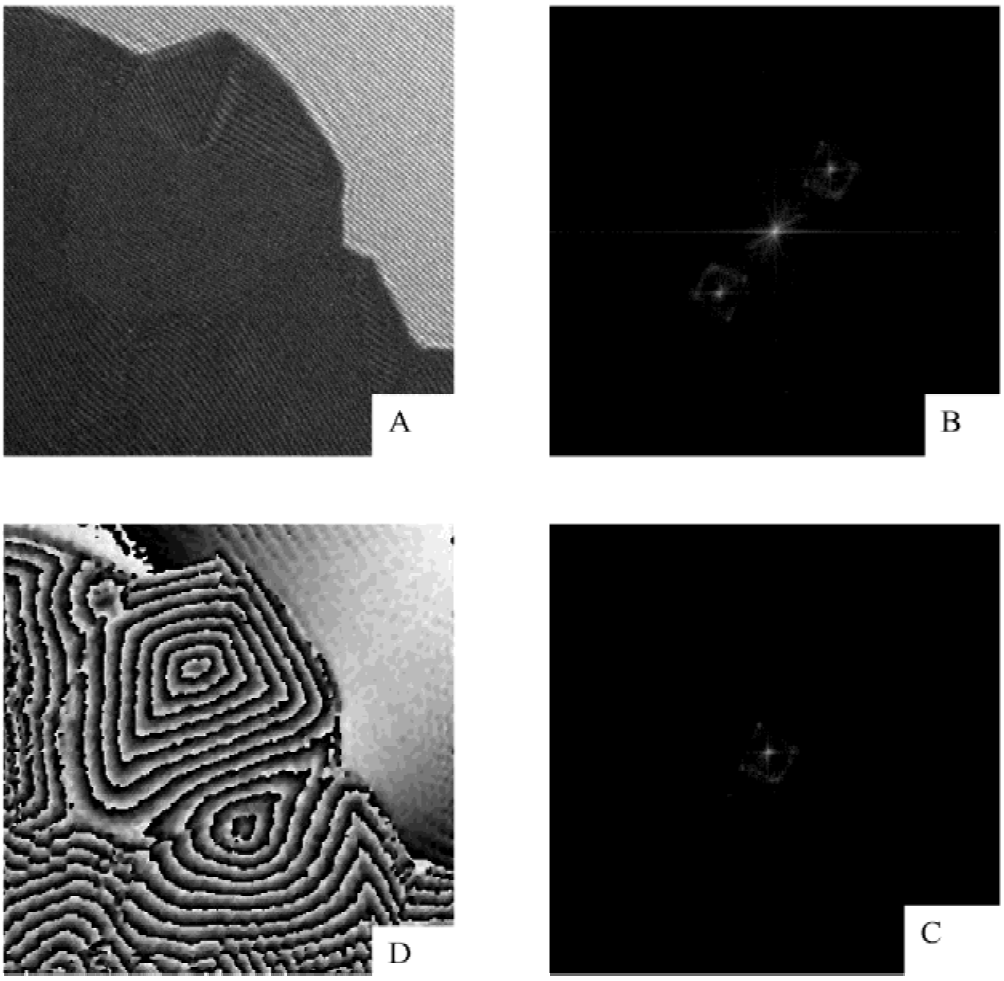

Figure 7. Step-by-step procedure to numerically reconstruct the phase from a hologram. **A:** Hologram. **B:** FFT of **A**, power spectrum with side bands. **C:** Cut and center **B**. **D:** Inverse FFT of **C** to obtain the phase map.

Discussion

To obtain the ripple wavelength in the LTEM observation of the nano-crystalline $Fe_{94}N_5Zr_1$ film (thickness 55 nm), the values of the ripple wavelength at different defocus values are measured and interpolated at zero defocus. In this particular case, this value gives a ripple wavelength of 400 ± 10 nm and deviation angle $\theta = 6 \pm 1.5°$. The experimental ripple wavelength can be compared with the theoretical value (λ_{th}) (Hoffmann, 1964) using the following theoretical formula for the ripple wavelength:

$$\lambda_{th} = 2\pi(A/K_u)^{1/2}(h \mp 1)^{-1/2}, \tag{5}$$

where A is the exchange constant, $K_u = MH_k/2$, the uniaxial anisotropy constant, and $h = H/H_k = HM/2K_u$ is the reduced field. Also the angle of deviation (θ_{th}) can be compared with the theoretical prediction, according to:

$$\theta_{th} = \frac{1}{4\pi^{1/2}} \frac{DK}{(2t)^{1/4}M^{1/2}} \frac{1}{\{AK_u(h+1)\}^{3/8}}, \tag{6}$$

where D is the mean grain size, t the thickness of the film, K the crystal anisotropy constant, M the saturation magnetization, K_u the uniaxial anisotropy constant, and $h = H/H_k$ is the reduced field. The difficulty when comparing the experimental data with theory stems from the fact that not all the physical parameters are accurately known. This is due to two reasons: Only values for pure iron are known and not for nano-crystalline iron, and second, even the values that are measured are often just estimates. For calculating λ_{th}, the following parameters are chosen: the exchange constant of (pure) iron is 1.49 10^{-11} J/m, the magnetization ranges

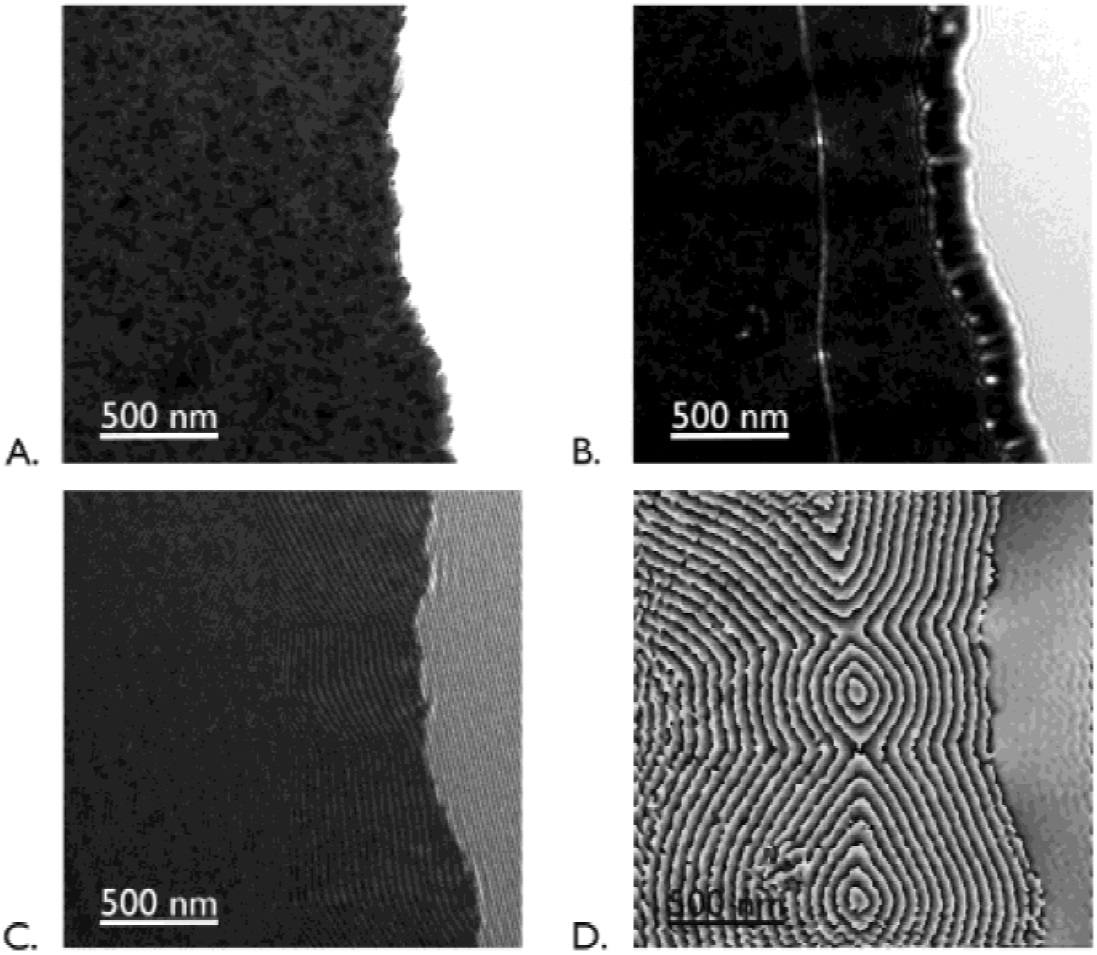

Figure 8. A structure image (**A**), a Lorentz–Fresnel image (**B**), a hologram (**C**), and the reconstructed phase (**D**) of nano-crystalline $Fe_{94}N_5Zr_1$.

from 1 to 1.5 Tesla, H_k is sample dependent and varies between 5 and 18 Oe. For calculating θ_{th}, besides the thickness and mean grain size of the sample, the crystal anisotropy constant for (pure) iron 4.7×10^4 J/m^3 is used. These values give a theoretical values of $\lambda_{th} = 1400$ nm and $\theta_{th} = 49°$, that is to say, both predicted values are much larger than the experimental findings. Besides the fact that the magnetic parameters are not precisely known, the principal reason of this discrepancy lies in the circumstance that the classical theory is probably not applicable to the case of nano-structured materials. One of the critical assumptions is that the effective crystalline anisotropy constant is much smaller than the uniaxial anisotropy constant ($K_{eff} \ll K_u$) but in the nano-crystalline material, both K_{eff} and K_u are of the same order of magnitude. Therefore, we suggest the following novel approach.

Clearly a quasi-periodic oscillation of the transversal component of the local magnetization is observed by LTEM. A set of almost parallel fringes in the under- or overfocused image is generated. In the classical theory of the LTEM imaging of micromagnetic ripple (Fuller and Hale, 1960) and in a diffraction approach (Wohlleben, 1967) the oscillations are one-dimensional and the absolute value of the magnetization has been assumed to be constant. These assumptions are rather questionable in nano-structured materials, and LTEM provides the possibility to elucidate the magnetic properties to a greater detail. It should be emphasized that we do not discuss any time dependence and consequently fluctuations are related only to space modulations either of magnetization in the film or of intensity in the LTEM image.

Due to the random orientations of the grains in nano-crystalline material, the magnetocrystalline anisotropy is averaged out to a large extent. A uniaxial anisotropy is induced during film deposition due to an applied magnetic field. The exchange interaction reduces the angular spread

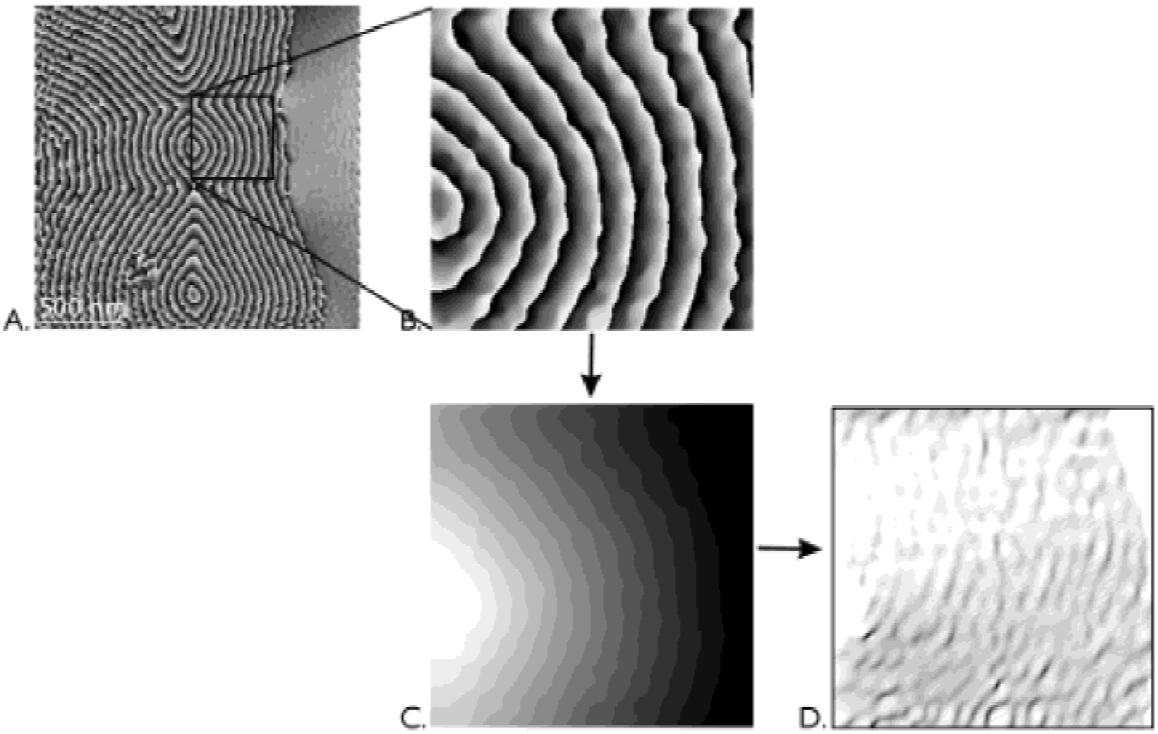

Figure 9. Example of determining the magnetic induction (**D**) from a hologram (**A**). A singularity-free section is selected (**B**), then the unwrapped phase is calculated (**C**), after which the derivative multiplied with a constant gives the magnetic induction (**D**).

of the magnetization vector due to the local residual crystalline anisotropy, leading to a correlated wiggling of the magnetization around the easy axis (EA), producing the ripples observed in Lorentz microscopy. This wiggling can be characterized by an amplitude of the transversal component of the magnetization, ΔM_y, which is a periodic function in the x direction. In the simplest approximation, we have

$$\Delta M_y = M\beta_0 \sin(2\pi x/\lambda_x), \tag{7}$$

where the EA is oriented along the x axis. The amplitude of the angle of the wiggling, β_0, is of the order of one degree and depends on the grain size and on the applied magnetic field (Chechenin et al., 2002). A transversal oscillation $\Delta M_y(y)$ is energetically unfavorable (Fuller and Hale, 1960) and the oscillation of $\Delta M_y(x)$ is called the longitudinal one. The component normal to the plane, ΔM_z, is suppressed due to the demagnetizing factor. The wiggling induces the internal stray field oriented parallel and antiparallel to the main magnetization direction. The magnitude of the stray field can easily be estimated by

$$\Delta B_{str,x} \approx -\pi M\beta_0^2 \cos(4\pi x/\lambda_x). \tag{8}$$

The presence of this mode induces an oscillating Lorentz force that moves the electrons perpendicular to the magnetization direction. However, the magnitude of this force is of one to two orders of magnitude less than the one induced by the transversal component of equation (7). Moreover, the period of the oscillation in equation (8) is half of that in equation (7), meaning that the mode of equation (8) will not produce any phase shift at the points of maximum phase shift due to the mode of equation (7). That leads to the conclusion that, in principle, the mode described by equation (8) only leads to a certain distortion of the phase contrast due to the mode given by equation (7). So far, the direction of magnetization vector oscillates but it is constant in magnitude. That is a traditional point of view. Now, we assume that the magnetization has a certain spread due to the nonaveraged crystalline anisotropy. In the case of random orientation of the crystallites, the residual crystalline component, ΔM_r, has a uniform orientation. In the presence of exchange interaction, the orientation is forced to correlate. However, the magnitude

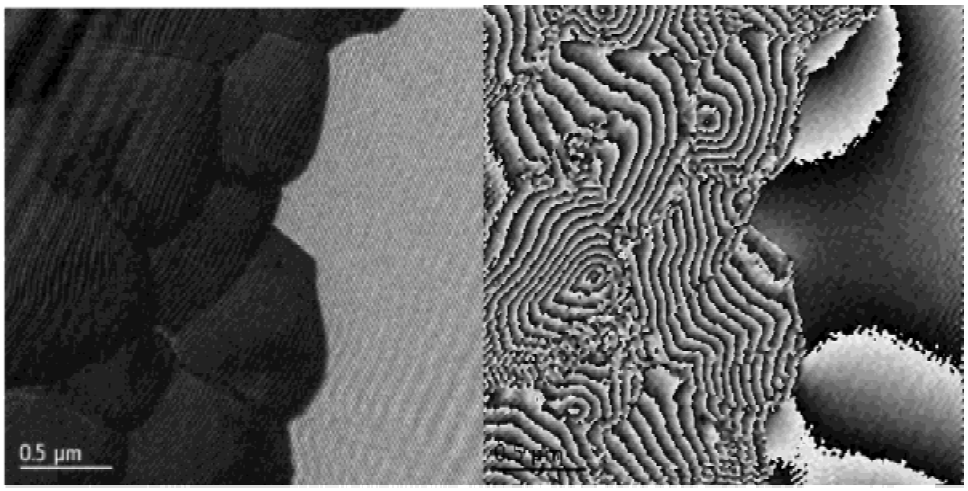

Figure 10. Hologram and phase image of nano-crystalline $Fe_{94}N_5Zr_1$.

of the magnetization is free to vary and the major effect is expected for the transverse variation of the x component. For simplicity, we again restrict ourselves to a simple harmonic oscillations, that is,

$$\Delta M_x = \Delta M_r \sin(2\pi y/\lambda_y). \tag{9}$$

Next, let us estimate the phase contrast in LTEM as produced by these magnetic features. The phase shift between two points of the image is determined by the magnetic flux through the area surrounded by lines connecting the corresponding points on the upper and lower surfaces of the films and the trajectories of electrons passing these points. If one of the points is at the origin of the coordinates, we write for the phase shift

$$\varphi(\mathbf{r}) = \frac{\pi}{\Phi_0}\int_0^t dz \int_0^{r(x,y)} \mathbf{B}(\mathbf{r},t)\cdot d\mathbf{S}, \tag{10}$$

where $\Phi_0 = 2e/\hbar = 2.06 \times 10^{-15}$ Wb, e is the electron charge, $\hbar$ is Planck's constant, t is the film thickness, $\mathbf{B}(\mathbf{r},t)$ is the local magnetic induction, and $d\mathbf{S}$ is an element of the area represented by the vector oriented along the normal to the area. For a uniform thickness and a uniform distribution of magnetization all through t equation (10) can be rewritten as

$$\varphi(\mathbf{r}(x,y)) = \frac{\pi}{\Phi_0}\, t \int_0^{r(x,y)} [B_y(x',y')\,dx' - B_x(x',y')dy'], \tag{11}$$

where

$$B_y = \Delta M_y \quad \text{and} \quad B_x = M + \Delta M_x + \Delta B_{strx}. \tag{12}$$

According to equations (7)–(9) the phase can be written as

$$\varphi(x,y) = \frac{\pi t}{\Phi_0}\left[\frac{M\beta_0\lambda_x}{2\pi}\left(1-\cos\frac{2\pi x}{\lambda_x}\right) - M_y - \frac{\Delta M_r \lambda_y}{2\pi}\left(1-\cos\frac{2\pi x}{\lambda_x}\right)\right], \tag{13}$$

where the contribution due to the mode described by equation (8) was neglected. The intensity variation of the electron image of LTEM can be evaluated using the Fourier transforms technique, that is (Chapman, 1984):

$$I(x',y') = \left|\iint F(k_x,k_y)T(k_x,k_y)e^{2\pi i(k_x x' + k_y y')}\,dk_x\,dk_y\right|^2, \tag{14}$$

where

$$F(k_x,k_y) = \iint f(x,y)\exp[-2\pi i(k_x x + k_y y)]\,dx\,dy, \tag{15}$$

is the Fourier transform of the exit electron wave function. Assuming that a plane electron wave enters the film $\exp(2\pi i k_0 z)$ where $k_0 = 1/\lambda_0$ and λ_0 is the electron wave length ($\lambda_0 = 2.5$ pm for the 200-kV electrons) and only the phase is modified by the magnetic film, the z-dependent

part of the $f(x, y)$ can be omitted in equations (14) and (15), leading to

$$f(x, y) = \exp[i\varphi(x, y)]. \tag{16}$$

Neglecting effects of the aperture and of the spherical aberration in the Fresnel mode of LTEM, the transfer function in equation (14) reads

$$T(k_x, k_y) = \exp[i\pi\Delta z\lambda_0(k_x^2 + k_y^2)], \tag{17}$$

where Δz is the defocus value ($-$ for overfocus, $+$ for underfocus). A nonzero value of Δz makes the ripple image observable. Next, equation (14) can be represented in the form of a convolution between $f(x, y)$ in equation (16) and the Fourier transform of $T(k_x, k_y)$, which yields

$$I(x', y') = \left| \int_{-\infty}^{\infty} dx \int_{-\infty}^{\infty} dy \exp[i\varphi(x, y)] \times \exp\left[-\pi i \frac{(x - x')^2 + (y - y')^2}{\Delta z\lambda_0}\right]\right|^2, \tag{18}$$

which can be easily integrated. Neglecting constant multipliers, we find

$$I(x, y) = I_x(x)I_y(y),$$

where

$$I_x(x) = 1 + 2S_x \cos(2\pi x/\lambda_x)\sin[\Delta z\lambda_0/(2\pi\lambda_x^2)] + 2S_x^2 \cos^2(2\pi x/\lambda_x)$$

$$I_y(y) = 1 - 2S_y \cos[(2\pi y - S_{y^2}\Delta z\lambda_0)/\lambda_x] \times \sin[\Delta z\lambda_0/(2\pi\lambda_y^2)] + 2S_y^2 \times \cos^2[(2\pi y - S_{y^2}\Delta z\lambda_0)/\lambda_y], \tag{19}$$

where $S_x = \Delta M_y t\lambda_x/2\Phi_0$, $S_y = \Delta M_r t\lambda_y/2\Phi_0$, and $S_{y2} = \pi Mt/\Phi_0$ are factors determining the contrast of the magnetic fluctuations in an LTEM image.

From the analysis presented in equations (7) to (19) follows that the intensity of the LTEM image will vary in both x and y directions, responding to different modes of magnetic oscillations (see equations (7) to (9)). The longitudinal oscillations of the transversal component of the magnetization described by equation (7) gives a phase contrast of the fringes that is oriented perpendicular to the main magnetization vector, as can be concluded from equations (7), (13), (18), and (19). The period of these fringes corresponds to λ_x. From the experimental observations follows that this period for different films may vary between 0.1 to 1.5 μm. If $S_x \ll 1$, then, from equation (19), the contrast of the ripple pictures reads

$$C_x = \frac{I_x(0) - I_x(\lambda_x/2)}{I_x(\lambda_x/4)} = 2S_x \sin\frac{\lambda_0\Delta z}{2\pi\lambda_x^2}. \tag{20}$$

The maximum contrast is reached when the defocusing conditions correspond to the sin term in $I_x(x)$ equals unity, leading to

$$C_x^{\max} = \Delta M_y \lambda_x t/\Phi_0. \tag{21}$$

This relation is similar to the one derived in Chechenin et al. (2002) but in equation (20) the defocusing Δz has been taken into account. The contrast depends linearly on Δz at small defocus values. The mode described by equation (9) produces a contrast that varies in the y direction, that is, along the ripple fringes. The period of this oscillation λ_y can be determined from the experiment. If $\Delta\xi_x = \Delta z\lambda_0/(2\pi\lambda_x^2)$ is the defocus argument of the sinusoidal function in $I_x(x)$ or C_x, then the corresponding argument of the sinusoidal function in $I_y(y)$ is $\Delta\xi_y = \Delta\xi_x(\lambda_x/\lambda_y)^2$. The contrast of $I_y(y)$ oscillations represented by

$$C_y = 2S_y \sin(\Delta\xi_y) = \Delta M_y t\lambda_y \sin(\Delta\xi_y)/(2\Phi_0) \tag{22}$$

is, in general, not optimal when the contrast of x oscillations is maximal. The magnitude of the variation of the magnetization vector can be estimated from the contrast described by equation (22).

The three-dimensional variation of the intensity in the image can now be calculated based on equation (19). To illustrate the outcome of this analysis, an example of the LTEM image with the ripple structure for the nano-crystalline Fe-Zr-N film is depicted in Figure 11, where a linear scan perpendicular to the ripple fringes (T profile) shows a quasi-periodic arrangement of the fringes (Fig. 11b). The analysis reveals the presence of two waves in the T scan with almost the same wavelength $\lambda_x \approx 0.45$ μm, which are shifted relative to each other by a distance slightly more than the half of the period. This type of fringes corresponds to a wiggling of the magnetization vector perpendicular to the easy axis, that is, the mode of equation (9) discussed above. The contrast is of the order of $C \approx 0.6$. This leads to

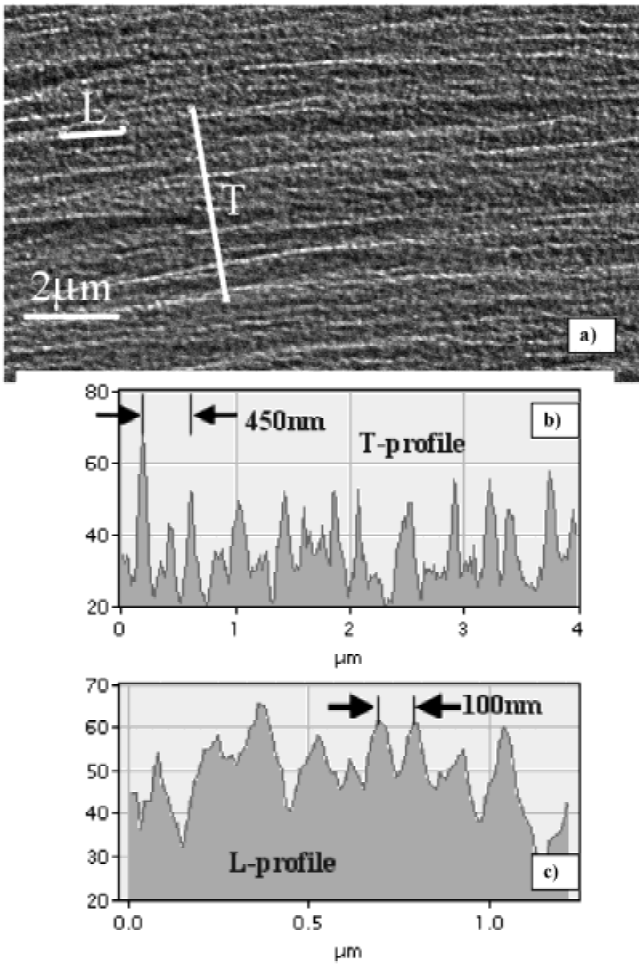

Figure 11. Analysis of the ripple structure in nano-crystalline $Fe_{94}N_5Zr_1$.

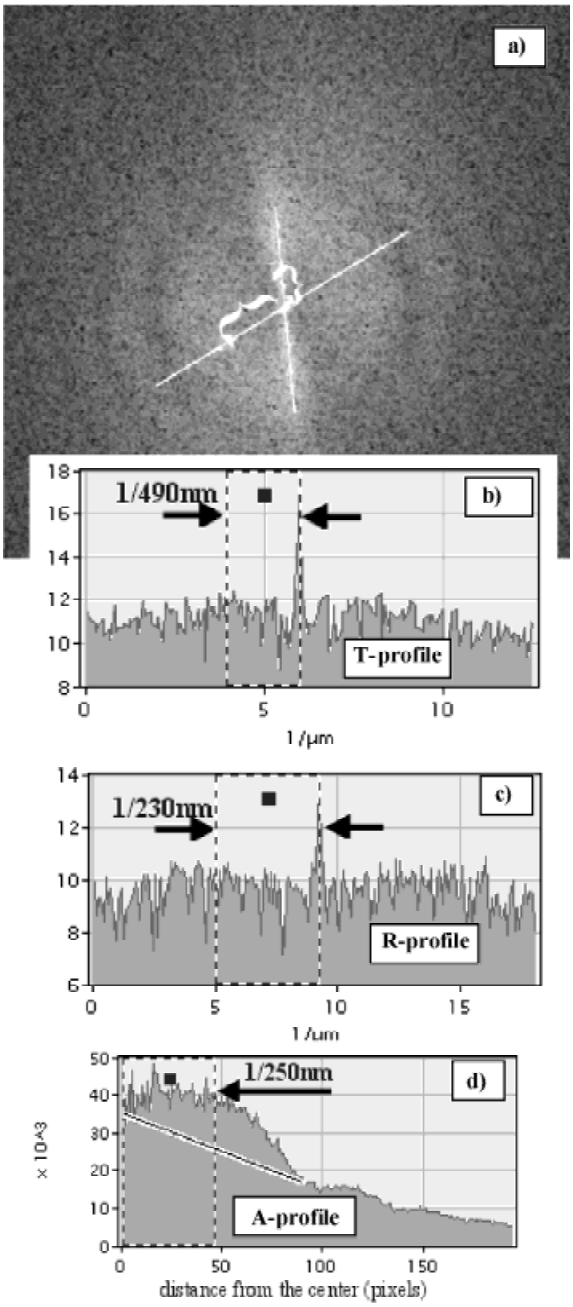

Figure 12. FFT analysis of the ripple structure in nano-crystalline $Fe_{94}N_5Zr_1$.

an amplitude of the transversal component $\Delta M_y \approx 23$ mT, or an amplitude of the wiggling angle $\beta_0 \approx 0.9°$.

As expected from our theoretical consideration, the intensity of the image also is inhomogeneous along the ripple direction. This is demonstrated in the longitudinal scan (L profile) in Figure 11c. This variation corresponds to the mode of equation (9) discussed in the previous section. The periodicity lies in between $\lambda_y \approx 0.1$–0.15 nm and the contrast $C \approx 0.2$. That gives the longitudinal fluctuation of the magnetization of the order of $\Delta M_x \approx 30$ mT, which is only slightly larger than the amplitude of the transversal component.

The Fourier transform of the image is depicted in Figure 12. The enhanced intensity of the FFT in the direction perpendicular to the fringes is clearly seen. However, the angular spread around this direction is significantly larger than $\beta_0 \approx 0.9°$. In addition, there is a significant background almost over the complete azimuth of the FFT. The radial intensity variations along the maximum of the intensity, corresponding to the T scan in Figure 12 and in an arbitrary direction (R scan) through the center of the FFT picture, are plotted in Figure 12b and c, respectively. Both profiles show a smooth and wide bump. In the T scan, the averaged radius corresponds to a periodicity of $\sim$0.49 μm and in the R scan to $\sim$0.23 μm, that is, of the same order of

magnitude as that of the image in Figure 11. In addition, in Figure 12d the radial profile is shown for azimuthally averaged FFT, which also shows a wide bump, positioned at an average radius corresponding to a periodicity of ~250 nm.

From an experimental viewpoint, it should be stressed that for the delineated analysis, special attention should be paid to the illumination convergence angle as well as to the value of the defocus. The ripples have to be nicely visible and this is accomplished at considerable defocus values. However, if the defocus is too extended, the measured ripple length will deviate largely. In this particular case reproducible values of the ripple period were obtained with a defocus of ±1000 to 4000 nm. From a determination of the ripple wavelength at different defocus values, the effect of the defocus on the measured ripple wavelength can be estimated. This produces the following results: Within a defocus bandwidth, the ripple wavelength is (approximately) constant. If the defocus is bigger than a certain value, the ripple wavelength rapidly increases, probably due to the change of the condenser lens current. The demand for a good ripple contrast is, in the case of the ripple deviation angle, even more compelling than in the case the ripple wavelength.

Conclusions

As a tribute to the scientific work of Professor Gareth Thomas, this paper delineates a new possibility of LTEM to study the structure property of functional materials by concentrating on the magnetic properties of soft magnetic films. We have shown that in contrast to the traditional point of view, not only does the direction of the magnetization vector in nano-crystalline $(Fe_{99}Zr_1)_{1-x}N_x$ films make a correlated small-angle wiggling, but also the magnitude of the magnetization modulus fluctuates. This fluctuation produces a rapid modulation in the LTEM image. Analysis of the ripple structure corresponds to an amplitude of the transversal component of the magnetization ΔM_y of 23 mT and a longitudinal fluctuation of the magnetization of the order of $\Delta M_x = 30$ mT. Also, an LTEM off-axis electron holography technique was explored as an alternative method for obtaining information about the magnetization. It turned out that electron holographic methods could also be used on these $(Fe_{99}Zr_1)_{1-x}N_x$ films to recover the phase. The derivative of the phase with respect to the position provided qualitative information about the magnetic induction in the x and y directions as a function of the position in the holographic image. For further quantification of the results obtained with the off-axis electron holographic method, a relation with the quantitative information of the LTEM technique will be explored in the future.

Acknowledgments

This work is part of the research program of the Priority Program on Materials of the Netherlands Organization of Research (NWO, The Hague) and supported by the Netherlands Foundation for Technical Sciences and the Netherlands Institute for Metals Research. Thanks are due to Professor Gareth Thomas for his stimulus provided over the years to the microscopy research in our Department of Applied Physics at the University of Groningen, the Netherlands.

References

Berkowitz, A.E., Mitchell, J.R., Carey, M.J., Young, A.P., Zhang, S., Spada, F.E., Parker, F.T., Hütten, A. & Thomas, G. (1992). Giant magneto resistance in heterogeneous Cu-Co alloys. *Phys Rev Lett* **68**, 3745–3748.

Chapman, J.N. (1984). The investigation of magnetic domain structures in thin foils by electron microscopy. *J Phys D: Appl Phys* **17**, 623–647.

Chechenin, N.G., Chezan, A.R., Craus, C.B., Vystavel, T., Boerma, D.O., De Hosson, J.Th.M. & Niesen, L. (2002). Microstructure of nanocrystalline FeZr(N)-films and their soft magnetic properties. *J Magn Magn Mater* (in press).

Chezan, A.R., Craus, C.B., Chechenin, N.G., Niesen, L. & Boerma, D.O. (2002). Structure and soft magnetic properties of Fe-Zr-N films. *Physica Status Solidi (a)* **189**, 833–841.

Cowley, J. (1992). Twenty forms of electron holography. *Ultramicroscopy* **41**, 335–348.

De Graef, M. (2000). Lorentz microscopy. In *Experimental Methods in the Physical Sciences, Volume 36: Magnetic Imaging and its Applications to Materials*, De Graef, M. & Zhu, Y. (Eds), pp. 27–67. New York: Academic Press.

Fuller, H.W. & Hale, M.E. (1960). Determination of magnetization distribution in thin films using electron microscopy. *J Appl Phys* **31**, 238–248.

Gabor, D. (1949). Microscopy by reconstructed wave-fronts. *Proc of the Roy Soc A* **197**, 454–487.

Gillies, M.F., Chapman, J.N. & Kools, J.C.S. (1995). Micromagnetic characteristics of single layer permalloy films in nanometre range. *J Magn and Magn Mater*, **140-144**, 721–722.

Grundy, P.J. & Tebble, R.S. (1968). Lorentz electron microscopy. *Adv Phys* **17**, 153–242.

Herrmann, M., Zweck, J. & Hoffmann, H. (1994). Observation and characterization of micromagnetic structures. *Int Conf Electron Microsc* **13**, 245–249.

Hoffmann, H. (1964). Quantitative calculation of the magnetic ripple of uniaxial thin permalloy films. *J Appl Phys* **35**, 1790–1798.

Hütten, A., Bernardi, J., Friedrichs, S. & Thomas, G. (1995). Microstructural influence on magnetic properties and giant magnetoresistance of melt-spun gold-cobalt. *Scripta Metall* **33**, 1647–1666.

Kooi, B.J., Vystavel, T. & De Hosson, J.Th.M. (2001). Nanostructure and giant magneto-resistive properties of granular systems. *J Nanosci Nanotechnol* **1**, 65–74.

McCartney, M.R., Dunin-Borkowski, R.E. & Smith, D.J. (2000). Electron holography and its application to magnetic materials. In *Experimental Methods in the Physical Sciences, Volume 36: Magnetic Imaging and its Applications to Materials*, De Graef, M. & Zhu, Y. (Eds), pp. 111–136. New York: Academic Press.

Midgley, P.A. (2001). An introduction to off-axis electron holography. *Micron* **32**, 167–184.

Thomas, G. & Goringe, M.J. (1979). *Transmission Electron Microscopy of Materials*. New York: Wiley and Sons.

Tonomura, A. (1999). *Electron Holography*. Berlin: Springer Series in Optical Sciences.

Vrenken, H., Kooi, B.J. & De Hosson, J.Th.M. (2001). Microstructure and properties of giant magneto-resistant granular $Au_{80}Co_{20}$ alloys. *J Appl Phys* **89**, 3381–3387.

Wohlleben, D. (1967). Diffraction effects in Lorentz microscopy. *J Appl Phys* **38**, 3341–3352.